http://dx.doi.org/10.5012/bkcs.2013.34.1.79

Model Prediction and Experiments for the Electrode Design Optimization of $LiFePO_4$/Graphite Electrodes in High Capacity Lithium-ion Batteries

Seungho Yu, Soo Kim, Tae Young Kim, Jin Hyun Nam,†,* and Won Il Cho*

*Center for Energy Convergence, Korea Institute of Science and Technology, Seoul 136-791, Korea. *E-mail: wonic@kist.re.kr*
†School of Mechanical and Automotive Engineering, Daegu University, Gyungsan 712-714, Korea
**E-mail: jinhnam@gmail.com*
Received August 27, 2012, Accepted October 5, 2012

$LiFePO_4$ is a promising active material (AM) suitable for use in high performance lithium-ion batteries used in automotive applications that require high current capabilities and a high degree of safety and reliability. In this study, an optimization of the electrode design parameters was performed to produce high capacity lithium-ion batteries based on $LiFePO_4$/graphite electrodes. The electrode thickness and porosity (AM density) are the two most important design parameters influencing the cell capacity. We quantified the effects of cathode thickness and porosity ($LiFePO_4$ electrode) on cell performance using a detailed one-dimensional electrochemical model. In addition, the effects of those parameters were experimentally studied through various coin cell tests. Based on the numerical and experimental results, the optimal ranges for the electrode thickness and porosity were determined to maximize the cell capacity of the $LiFePO_4$/graphite lithium-ion batteries.

Key Words : $LiFePO_4$, Battery design parameter, Electrode thickness, Porosity, Electrochemical model

Introduction

With the growing popularity of electric vehicles (EVs) and hybrid electric vehicles (HEVs), rechargeable lithium-ion batteries have received increased research attention. Compared with the low-power batteries currently used for portable electronic devices, automotive batteries are required to provide higher power capability, lower heat dissipation, and better safety characteristics (due to the larger cell volume). To improve these characteristics, lithium iron phosphate ($LiFePO_4$) has been investigated by multiple. While $LiFePO_4$ has a theoretical charge capacity (specific energy) lower than that of the currently used materials ($LiCoO_2$, $LiMn_2O_4$), $LiFePO_4$ has several advantages, including a low cost, a good safety profile, low toxicity, and a long cycle life, that make $LiFePO_4$ a promising candidate for use in cathode materials, especially for EV and HEV applications.

In an attempt to improve the power performance of lithium-ion batteries using $LiFePO_4$, researchers have investigated the use of carbon coating[1-3] or metallic element doping[4-6] to increase the electrical conductivity, or by using nano-sized $LiFePO_4$ particles[7,8] to decrease the ionic diffusion distance. In addition, optimization studies have also been conducted to determine the optimal ranges for the $LiFePO_4$ battery design parameters, including the particle size, the electrode thickness, the porosity (density), and the conductor ratio (conductor weight fraction).[9-12] The optimization of the battery design parameters based solely on experimental approaches is difficult, not to mention time-consuming.[13] To facilitate the optimization, numerical modeling can help to accelerate the process by elucidating the effects of the electrode design parameters.

Many numerical studies have been conducted to investigate the effects of various design parameters for lithium-ion batteries.[14-17] Many of these numerical studies are based on the mathematical models developed by Newman *et al.*.[18-21] For the modeling of $LiFePO_4$ materials, Srinivasan and Newman[22,23] proposed a shrinking core model that demonstrated a good agreement between the experimental and predicted results for $LiFePO_4$/natural graphite lithium-ion batteries. More physically accurate models have been proposed based on the phase transition with an anisotropic diffusion in the $LiFePO_4$ materials.[24-26] However, in order to optimize design parameters using continuum level simulations along with experimental results, the primary model developed by Newman *et al.*[18-21] can be used to investigate and predict the effect of the design parameters such as the electrode thickness and density.

Among the various design parameters for the $LiFePO_4$ lithium-ion batteries, this study investigated the electrode thickness and porosity (AM density), aiming to obtain a high discharge capability for use in EV or HEV applications. A numerical simulation was conducted to first identify the general performance trends of the $LiFePO_4$/graphite lithium-ion batteries with respect to the electrode thickness and porosity. A one-dimensional (1D) electrochemical model coupled with a spherical particle diffusion model was developed using the Newman models.[18-23] The performance trends were experimentally investigated by performing the cell tests. While the recent modeling work by Newman *et al.*[23] to design $LiFePO_4$/natural graphite lithium-ion batteries systems may not correspond well with experimental results, we improved this modeling approach using a careful reexamination of the experimental results to further optimize our numerical simulations for the design parameters. From a practical point of view, our experimental and simulation

studies have an improved accuracy and can be immediately adapted to the lithium-ion battery industries to determine the optimal ranges for the electrode thickness and porosity.

Methods

Experimental. The AMs for the experiment, $LiFePO_4$ and graphite (supplied by Samsung SDI Corp., LTD) were in powder form and had an average particle size of 150 nm and 10 μm, respectively. The cathode slurry was prepared by mixing the $LiFePO_4$ powder with a polyvinylidene fluoride (PVDF) binder and an acetylene black (AB) conductor powder in an *N*-methyl pyrrolidone (NMP) solvent. Both the AB and PVDF were added to the slurry to a concentration of 5 wt %. The anode slurry was prepared by mixing the graphite powder with the PVDF binder with a mixing ratio of 95 wt % for the AM and 5 wt % for the PVDF. The slurries were coated onto an Al foil and a Cu foil to form a cathode and an anode. Tthe electrodes were dried in an oven at 80 °C for 4 h.

The thickness of the $LiFePO_4$ electrodes were varied from 60 μm to 120 μm by both controlling the height of the doctor blade and changing the amount of the NMP added to the slurry. The thicknesses of the graphite anode were determined to be proportional to the corresponding capacity of the $LiFePO_4$ electrode assembled in a full cell. The density of the AM in the electrode was determined by varying the compression ratios with a mechanical calendaring process. The values of the density were approximately 1.95, 2.05, and 2.23 g/cm^3. After compaction to a certain density, the electrodes were dried in a vacuum oven at 80 °C for 12 h.

A $LiFePO_4$ electrode and a graphite electrode were placed in a standard coin cell construction (2032 type, Hoshen), and an ethylene carbonate/dimethyl carbonate/ethylmethyl carbonate (1:1:1 vol %) solution with 1 M $LiPF_6$ was added as the electrolyte. The electrochemical behaviors of these cells were tested for several galvanostatic charge/discharge cycles using a battery cycler (Maccor 4000, Maccor Inc., USA) with a cut-off voltage range from 2.5-4.0 V. The applied charge/discharge current rate ranged from 0.1C to 2C.

Numerical. Numerical simulations were used to investigate the electrochemical behaviors during the discharge cycle of the $LiFePO_4$/graphite cells. A numerical code was developed based on the mathematical model proposed by the Newman group.[18-23] This code modeled the electrochemical and transport processes in a 1D lithium-ion battery formed with multiple layers, including a separator layer, electrode layers, and current collector layers. The mass transport inside the AM particles was also included in the code using spherical coordinates. Using the finite difference method with implicit time marching, the numerical code was used to solve for the following main variables: solid potential, F1, the electrolyte potential, Φ_2, the electrolyte concentration, c, the solid concentration, c_s, and the local current density, j_i.

The governing equation for the solid phase potential, Φ_1, in the negative or positive electrode ($i = n, p$) is expressed as

$$\sigma_{eff,i}\frac{\partial^2\Phi_1}{\partial x^2} = a_i F j_i, \tag{1}$$

wher $\sigma_{eff,i}$ (S/m) is the effective electronic conductivity of the solid phas a_i (m^{-1}) is the specific surface area of the AM particles, F is the Faraday's constant (96,487 C/mol), j_i and (mol/m^2-s) is the local current density (the intercalation flux of the lithium ions on the surface of the AM particle). The concentrated solution theory was used to describe the solution phase potential, Φ_2, in the negative electrode, the separator, or the positive electrode ($i = n, s, p$)

$$-\sigma_{eff,i}\frac{\partial\Phi_1}{\partial x} - \kappa_{eff,i}\frac{\partial\Phi_2}{\partial x} + \frac{2\kappa_{eff,i}RT}{F}(1-t_+)\frac{\partial \ln c}{\partial x} = I \tag{2}$$

where $\kappa_{eff,i}$ (S/m) is the effective ionic conductivity of the electrolyte phase, R is the universal gas constant (8.314 J/mol-K), T (K) is the absolute temperature, t_+ is the transference number of the lithium ions in the electrolyte, and c (mol/m^3) is the electrolyte concentration.

The concentration of the lithium ions in the electrolyte, c, for all domain is governed by

$$\varepsilon_i\frac{\partial c}{\partial t} = D_{eff,i}\frac{\partial^2 c}{\partial^2 t} + a_i(1-t_+)j_i \tag{3}$$

where ε_i is the porosity and $D_{eff,i}$ (m^2/s) is the effective electrolyte diffusion coefficient in the corresponding layer. The lithium concentration inside the AM particles, c_s, in the negative or the positive electrode ($i = n, p$) is calculated using Fick's diffusion equation in spherical coordinates

$$\frac{\partial c_s}{\partial t} = \frac{D_{s,i}}{r^2}\frac{\partial}{\partial r}\left(r^2\frac{\partial c_s}{\partial r}\right)_i \tag{4}$$

where $D_{s,i}$ (m^2/s) is the diffusion coefficient for the lithium ions inside the AM particle. The local current density for the negative or the positive electrode ($i = n, p$) is calculated using the Butler-Volmer equation

$$j_i = 2k_i(c_{s,\max,i} - c_{s,i}|_{r=R_i})^{0.5}(c_{s,i}|_{r=R_i})^{0.5}c^{0.5}\sinh\left[\frac{0.5F}{RT}(\Phi_1 - \Phi_2 - U_i)\right] \tag{5}$$

where k_i (mol/(mol/m^3)$^{1.5}$) is the reaction rate constant of the electrode, $c_{s,\max,i}$ (mol/m^3) is the maximum concentration of the lithium ions in the AM particle, U_i (V) is the open-circuit potential of the electrode. Eqs. (1)-(5) can be effectively illustrated as shown in Table 1. The relevant boundary conditions for Eqs. (1)-(5) are provided in Table 2.

Table 3 shows the correlations for the effective conductivity and diffusivity, the active surface area per unit volume, and the equilibrium potential for the negative and the positive electrodes. The physical parameters required for the simulations are summarized in Table 4 and Table 5. The electrode parameters provided in Table 5, including the volume ratio, the AM density, and the theoretical capacity at various thicknesses and porosities, were determined experimentally.

Table 1. Governing equations

Electrochemical reactions	Governing equation	Region
Solid phase conduction	$\sigma_{eff,i}\frac{\partial^2\Phi_1}{\partial x^2} = a_i F j_i$	Electrodes
Electrolyte phase conduction	$-\sigma_{eff,i}\frac{\partial\Phi_1}{\partial x} - \kappa_{eff,i}\frac{\partial\Phi_2}{\partial x} + \frac{2\kappa_{eff,i}RT}{F}(1-t_+)\frac{\partial \ln c}{\partial x} = I$	Electrodes, Separator
Electrolyte phase diffusion	$\varepsilon_i\frac{\partial c}{\partial t} = D_{eff,i}\frac{\partial^2 c}{\partial^2 x} + a_i(1-t_+)j_i$	Electrodes, Separator
Solid phase diffusion	$\frac{\partial c_s}{\partial t} = \frac{D_{s,i}}{r^2}\frac{\partial}{\partial r}\left(r^2\frac{\partial c_s}{\partial r}\right)_i$	Electrodes
Activation reaction	$j_i = 2k_i(c_{s,\max,i}-c_{s,i}\vert_{r=R_i})^{0.5}(c_{s,i}\vert_{r=R_i})^{0.5}c^{0.5}\sinh\left[\frac{0.5F}{RT}(\Phi_1-\Phi_2-U_i)\right]$	Electrodes

i = n (negative), p (positive), s (separator)

Table 2. Boundary condition

Boundary conditions	Electrode-separator interface	Electrode-current collector interface
Solid potential, Φ_1	$-\sigma_{eff,i}\frac{\partial\Phi_1}{\partial x} = 0$	$-\sigma_{eff,i}\frac{\partial\Phi_1}{\partial x} = I$
Electrolyte potential, Φ_2	Continuous	$-\kappa_{eff,i}\frac{\partial\Phi_2}{\partial x} = 0$
Concentration, c	Continuous	$-D_{eff,i}\frac{\partial c}{\partial x} = 0$
Solid concentration, c_s	$\left.\frac{\partial c_s}{\partial r}\right\vert_{r=0} = 0, j_i = -D_{s,i}\left.\frac{\partial c_s}{\partial r}\right\vert_{r=R_i}$	

Table 3. Expressions used in the battery simulation

$\sigma_{eff,i} = \sigma_i(1-\varepsilon_i-\varepsilon_{f,i}-\varepsilon_{p,i})$, $i = n, p$

$\kappa_{eff,i} = \varepsilon_i^{1.5}\,(0.0911 + 1.910c - 1.052c^2 + 0.1554c^3)$, $i = n, s, p$

$D_{eff,i} = D_i\varepsilon_i^{1.5}$, $i = n, s, p$

$a_i = \frac{3}{R_i}(1-\varepsilon_i-\varepsilon_{f,i}-\varepsilon_{p,i})$, $i = n, p$

$U_n = \frac{-14.61x^2 \times 13.71x}{-55.03x^2+108.85x-3.495}$, $x = c_{s,n}/c_{s,n,\max}$

(for $0.07 < x < 0.95$)

$U_p = \frac{3.413}{1+0.0498x^{13.36}-21.95x^{83.42}}$, $x = c_{s,p}/c_{s,p,\max}$

(for $0.05 < x < 0.95$)

Table 4. Physical parameters used in the battery simulation

Parameter	Graphite	$LiFePO_4$
Radius of particles[a]	10 μm	150 nm
Diffusion coefficient[b] (m^2/s)	8×10^{-14}	6×10^{-18}
Reaction rate constant[b] (mol/s·m^2) [(mol/ m^3)$^{-1.5}$]	5×10^{-11}	3.5×10^{-13}
Conductivity[a] (S/m)	100	11.8
Initial SOC[a]	0.9	0.1
Electrolyte diffusion coefficient (m^2/s)	3×10^{-10}	
Initial concentration[a] (mol/m^3)	1,000	
Transport number	0.363	
Thickness of separator[a] (μm)	25	
Separator porosity[a]	0.55	
Faraday's constant (C/mol)	96,487	
Temperature (K)	298.15	
Universal gas constant (J/mol·K)	8.314	

[a]Measured values. [b]Model fits

Table 5. Electrode parameters used in the battery simulation

Electrode	Porosity (%)	AM (vol %)	AB (vol %)	PVDF (vol %)	AM density (g/cm^3)	Theoretical capacity (mAh/cm^2) @100 μm
Positive	31	56.76	5.822	6.414	2.04	3.474
electrode	25	61.7	6.328	6.972	2.22	3.776
Negative electrode	34	61.95	0	4.05	1.40	5.180

Results and Discussion

Simulation. Numerical simulations were performed to first investigate the effects of the electrode thickness and porosity on the discharge capacity of the $LiFePO_4$/graphite lithium-ion batteries below a 2 C current rate. The discharge curves were recorded during the experimental cell tests with a $LiFePO_4$ electrode with a 76 μm thickness and a 2.05 g/cm^3 AM density (the porosity was estimated to be approximately 0.31). These results were used to determine the model parameters provided in Table 3. As shown in Figure 1, the comparisons between the measured and the simulated discharge curves at current rates of 0.5 C, 1 C, and 2 C show relatively good agreement, indicating the validity of the present simulations. In Table 3, the diffusion coefficient and the reaction rate constant for the electrodes were determined from the curve fitting. The solid phase conductivity for the electrodes was measured by using the 4-point probe techni-

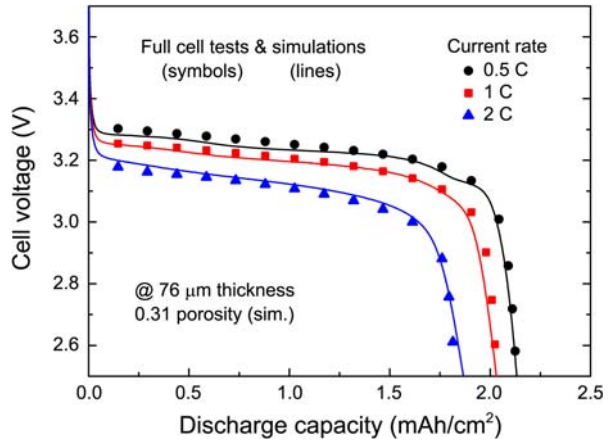

Figure 1. Comparison of the measured (lines) and the predicted (symbols) discharge curves for a $LiFePO_4$/graphite lithium-ion battery.

que. The particle size of the $LiFePO_4$ and the graphite were estimated from the SEM images. The other parameters in Table 3 were obtained either from the specification and operating conditions or from references in the literatures.[12,13]

The discharge behaviors of the $LiFePO_4$/graphite batteries were calculated for the electrode porosities of 0.31 and 0.25 with varying electrode thicknesses. In Table 4, the cathode parameters for the two porosity cases are provided. Figure 2 shows the dependency of the discharge capacity on the electrode thickness at a constant porosity of 0.31 as predicted by the numerical simulation. In Figure 2(a), the voltage drop increases as the cathode thickness exceeds 110 μm at a current rate of 1 C, leading to a significant capacity loss. The transport limitations in the electrolyte phase may be the dominant reason for the voltage drop and the capacity loss, becoming significant with increasing electrode thickness. At a 2 C current rate, the electrodes with a thickness greater than 85 μm experience a significant voltage drop and a capacity loss as shown in Figure 2(b). High current rates require high ion transport rates, leading to increased transport limitations in the electrolyte phase at small cathode thicknesses.

Figure 3 shows the simulated discharge curves for the various electrode thicknesses at a constant porosity of 0.25. Compared with Figure 2, the porosity is reduced by approximately 20% from 0.31 to 0.25. Similar to the trend observed in Figure 2, the voltage drop and the capacity loss shown in Figure 3 also increase significantly with increasing electrode thickness past a certain critical electrode thickness. This critical thickness value may result from severe transport limitations in the electrolyte phase. The critical thickness

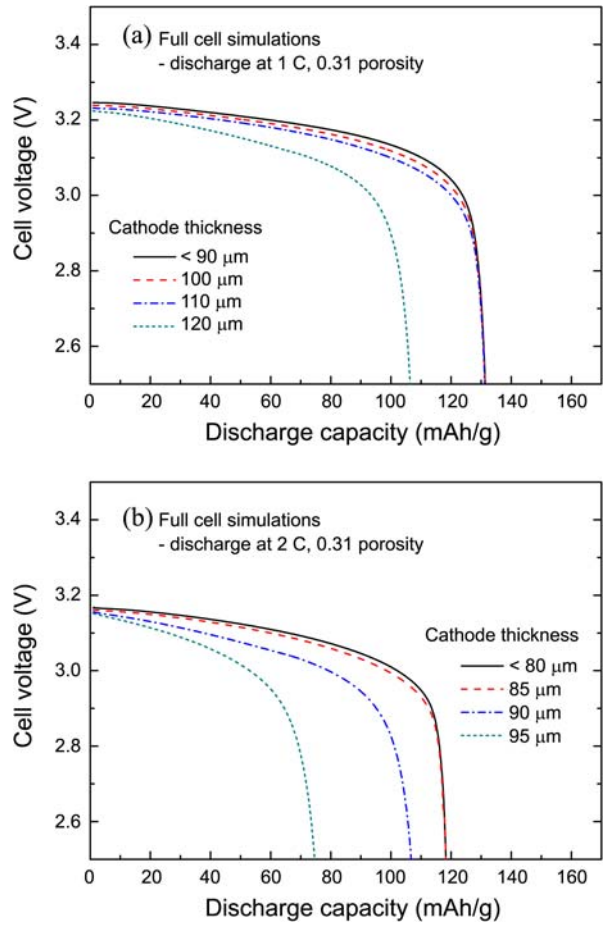

Figure 2. The predicted discharge curves at various electrode thicknesses with a constant porosity of 0.31: for current rates of (a) 1 C and (b) 2 C.

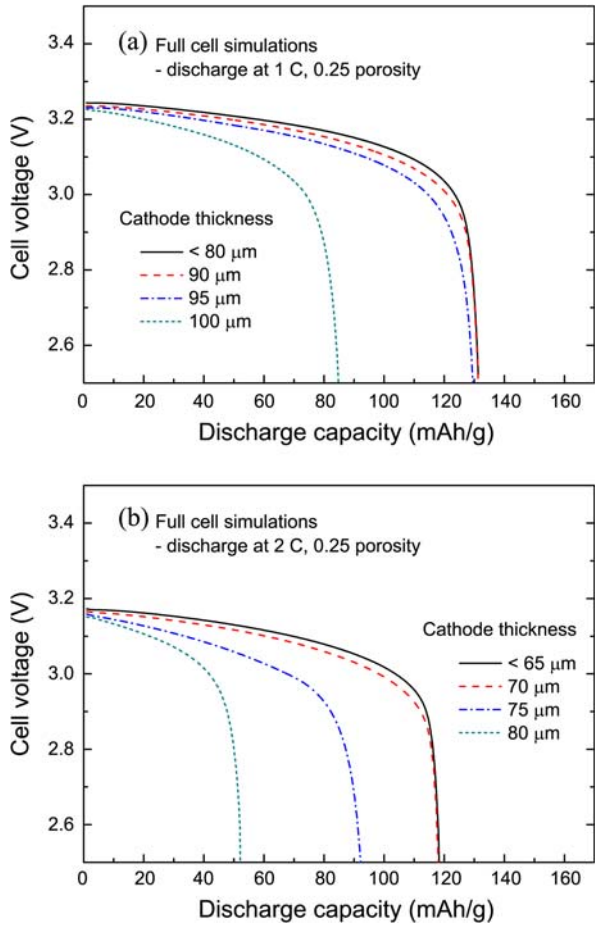

Figure 3. Predicted discharge curves at various electrode thicknesses with a constant porosity of 0.25 for current rates of (a) 1 C and (b) 2 C.

value is expected to be strongly dependent on the electrode porosity and current rate. In Figure 3(a) and (b), the critical thicknesses for an electrode porosity of 0.25 were estimated to be approximately 95 μm for a 1 C rate and 70 μm for a 2 C rate. As shown in Figure 2, the electrodes with the porosity of 0.31 indicate that the critical thicknesses are approximately 110 μm for a 1 C rate and 85 μm for a 2 C current rate. In summary, decreasing electrode porosities with increasing current rates resulted in small values for the critical thickness.

To compare the cell capacities, the discharge capacity per unit area should be considered. As shown in Table 4, the theoretical area specific discharge capacities were estimated to be 3.474 mAh/cm^2 for a porosity of 0.31 and 3.776 mAh/cm^2 for a porosity of 0.25 for the electrode thickness of 100 ìm, indicating that electrode compression was required to increase the volumetric energy density of the lithium-ion batteries. However, the dense electrodes may have caused a severe voltage drop at the high current rates, reducing the discharge capacity.

The area specific discharge capacity predicted by the numerical simulation is presented in Figure 4. The effects of the AM density (porosity) and the electrode thickness are well observed. Figure 4 is a rearrangement of Figures 2 and 3 in terms of the area specific discharge capacity. The AM densities are shown in Table 4, with values of 2.04 g/cm^3 corresponding with the electrode porosity of 0.31 and 2.22 g/cm^3 corresponding with a porosity of 0.25. For small electrode thicknesses, the discharge capacity is reasonably proportional to the electrode thickness and the AM density (Fig. 4). In this region, the transport limitations in the electrolyte phase are believed to be negligible as the dominant decrease in voltage stems from the solid phase diffusion loss in the AM particles.

As the electrode thickness increases to be greater than the critical values, the discharge capacity decreases rapidly, primarily due to the transport limitations in the electrolyte phase. To obtain a high discharge capacity at a 1 C current rate, the curves in Figure 4(a) suggest that the electrode thicknesses should be less than 110 μm for an AM density of 2.04 g/cm^3 or less than 95 μm for an AM density of 2.22 g/cm^3. The critical thickness was reduced from 110 μm to 95 μm with the increased transport limitations in the dense electrodes. The critical thickness was further reduced with increasing transport limitations at high current rates. At a 2 C rate, the critical thickness was 85 μm for an AM density of 2.04 g/cm^3 and 70 μm for an AM density of 2.22 g/cm^3.

The concentration profiles for the lithium ions in the electrolyte at the end of the discharge process (at the instance the discharge voltage reaches the cut-off voltage) are shown in Figure 5, using the same simulated conditions for Figure 2(a) or Figure 4(a) (1 C current rate and 2.04 g/cm^3 AM density). As shown in Figure 5, the concentration of the lithium ions decreased from the anode to the separator and from the separator to the cathode. The concentration in the anode increased with the deintercalation of the lithium ions from the AM particles. Likewise, the concentration in the cathode decreased with the intercalation of the lithium ions into the AM particles. As shown in Figure 5, the slope of the lithium-ion concentration increases with increasing electrode thickness as the transport of the lithium ions in the electrolyte phase becomes restricted in the thick electrodes. The low lithium-ion concentration in the cathode (along

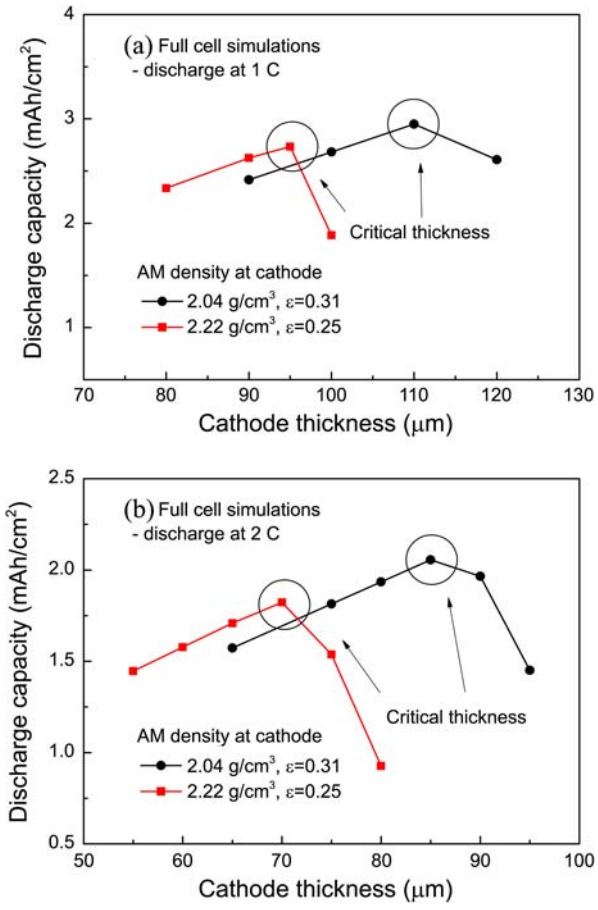

Figure 4. Predicted discharge capacity as a function of the electrode thickness for porosities of 0.31 (2.04 g/cm^3 AM density) and 0.25 (2.22 g/cm^3) for current rates of (a) 1 C and (b) 2 C.

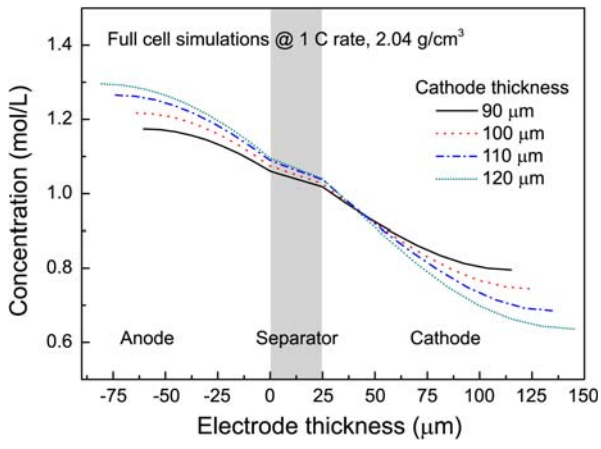

Figure 5. The lithium-ion concentration profiles in the electrolyte upon reaching the cut-off voltage (2.5 V) for the AM density of 2.04 g/cm^3 at the current rate of 1 C.

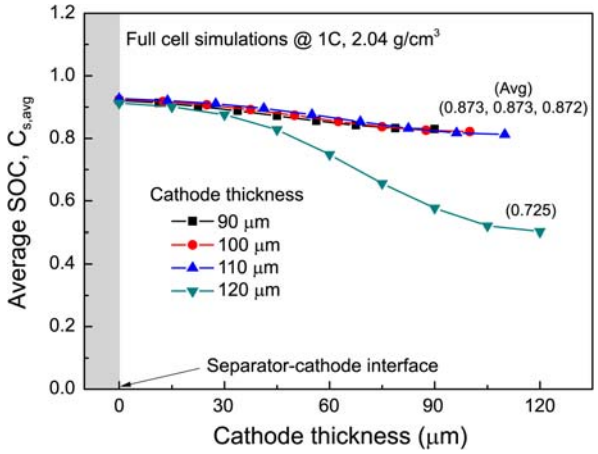

Figure 6. The average SOC profiles in the cathode upon reaching the cut-off voltage (2.5 V) for the AM density of 2.04 g/cm^3 at the current rate of 1 C.

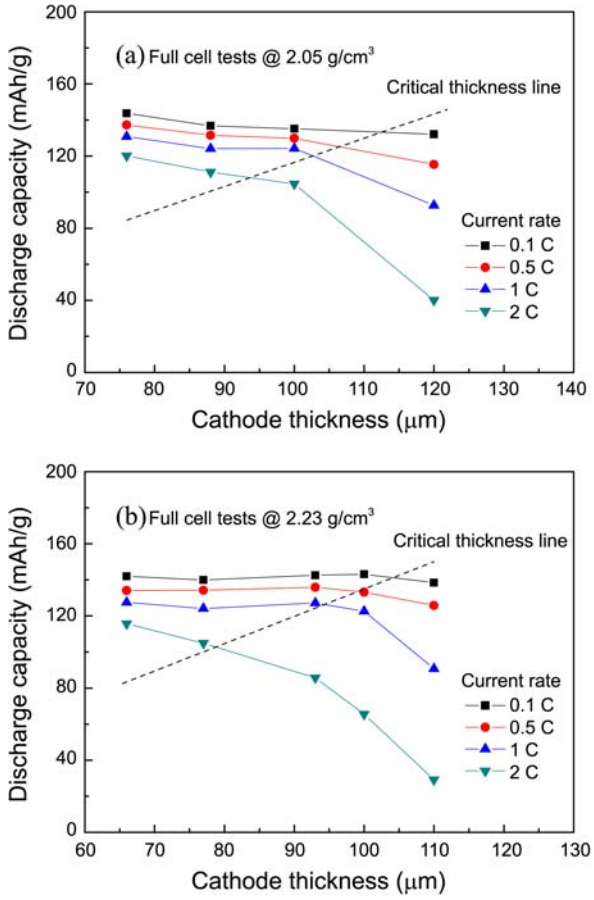

Figure 7. The measured discharge capacity per AM mass (mAh/g) for various cathode thicknesses and current rates: for the AM densities of (a) 2.05 g/cm^3 and (b) 2.23 g/cm^3.

with the high concentration in the anode) observed in the thick electrodes resulted in additional voltage drops that reduced the discharge capacity.

As shown in Figure 6, the average SOC in the cathode at the end of the discharge process was analyzed to investigate the effective utilization of the $LiFePO_4$ AM particles. The simulated conditions were the same as those used in Figure 5, such as a current rate of 1 C and an AM density of 2.04 g/cm^3. The average SOC denotes the degree of the lithium-ion intercalation in the AM particles. With a value of 0.1 at the fully charged state, the average SOC in the cathode continuously increased during the discharge process, with the intercalation of the lithium ions. An analysis of Figure 6 indicated that the average SOC at the end of the discharge process was relatively uniform at approximately 0.9 for electrode thicknesses smaller than the critical thickness of 110 μm. With the ion transport limitations, the average SOC had high values near the separator and low values near the current collector. With the cathode thickness exceeding the critical value, the average SOC was non-uniform, with the cell voltage prematurely dropping to values below the cut-off voltage (2.5 V) before the intercalation sites in the $LiFePO_4$ AM particles were fully utilized.

Cell Tests. The cell tests were conducted with the $LiFePO_4$/graphite lithium-ion batteries to investigate the observed trend of the discharge capacity around the critical electrode thickness. The $LiFePO_4$ cathodes with thicknesses ranging from approximately 70 μm to 120 μm and AM density values similar to those in the simulated conditions were fabricated for the cell tests. In this study, the minimum required discharge capacity was set to 120 mAh/g or 2.5 mAh/cm^2 at a 1 C current rate. The electrode design parameters leading to a capacity higher than this value were assumed to be in the optimal ranges. Figure 7 shows the discharge capacity per AM mass (mAh/g) measured during the cell tests. The AM mass specific discharge capacity decreased with the current rate, indicating that an increased amount of energy stored in the batteries can be used at small operating current rates. At a current rate below 0.5 C, no significant capacity loss was observed for an electrode thickness of 120 μm, as shown in Figure 7(a) and (b). With a constant discharge capacity per AM mass, increasing the electrode thickness resulted in an increased area specific discharge capacity.

As shown in Figure 7, the discharge capacity loss for the thick electrodes became noticeable with increases in the current rate to 1 C and 2 C. This reduction in the AM mass specific discharge capacity was related to the transport limitations in the electrolyte phase that resulted in a decreased area specific discharge capacity even with the large electrode thickness. The critical thickness line shown in Figure 7(a) can be used to determine the proper range for the electrode thickness at the AM density of 2.05 g/cm^3, *i.e.*, approximately 100 μm for a 1 C current rate and 90 μm for a 2 C current rate. With values below this critical electrode thickness, the discharge capacity can be maintained at values higher than approximately 135 mAh/g, 125 mAh/g, and 110 mAh/g for the 0.5 C, 1 C, and 2 C current rates, respectively. Compared with the capacity at the 0.1 C rate, these capacities correspond with the capacity efficiency of approximately 95%, 89%, and 79% at the 0.5 C, 1 C, and 2 C rates, respectively.

As shown in Figure 7(b), the discharge capacity of the

dense electrodes exhibited higher capacity losses with increasing electrode thickness. At the AM density of 2.23 g/cm^3, the critical thickness decreases to approximately 95 μm for the 1 C current rate and 80 μm for the 2 C current rate. Beyond this critical electrode thickness, the discharge capacity loss dropped significantly. In summary, an analysis of Figure 7 suggests that the electrode thickness and the AM density should be properly designed to avoid a severe capacity loss, especially for the thick electrodes and high current rate applications.

The experimental results for the discharge capacity per unit area (mAh/cm^2) are shown in Figure 8 for the three AM densities of 1.95 g/cm^3, 2.05 g/cm^3, and 2.23 g/cm^3 with various electrode thicknesses. As shown in Figure 8, the discharge capacity determined from the cell tests also was consistent with the simulated trends around the critical electrode thickness. The area specific discharge capacity increased in proportion to the electrode thickness, dropping rapidly as the electrode thickness exceeded the critical value. Using Figure 8, the critical electrode thickness was estimated to be 125 μm for an AM density of 1.95 g/cm^3, 110 μm for 2.05 g/cm^3, and 100 μm for 2.23 g/cm^3 at a 1 C current rate. These values are similar to the predicted critical thicknesses at a 1 C current rate using the numerical simulation (approximately 110 μm for a 2.04 g/cm^3 AM density and 95 μm for 2.22 g/cm^3). The critical electrode thickness decreased upon increasing the current rate to 2 C, *i.e.*, approximate values of 115 μm for 1.95 g/cm^3, 100 μm for 2.05 g/cm^3, and 80 μm for 2.23 g/cm^3, as shown in Figure 8.

From the minimum required discharge capacity of 2.5 mAh/cm^2 at a 1 C current rate, the optimal electrode thickness was determined to be 115 μm, 100 μm, and 90 μm for 1.95 g/cm^3, 2.05 g/cm^3, and 2.23 g/cm^3, respectively. At

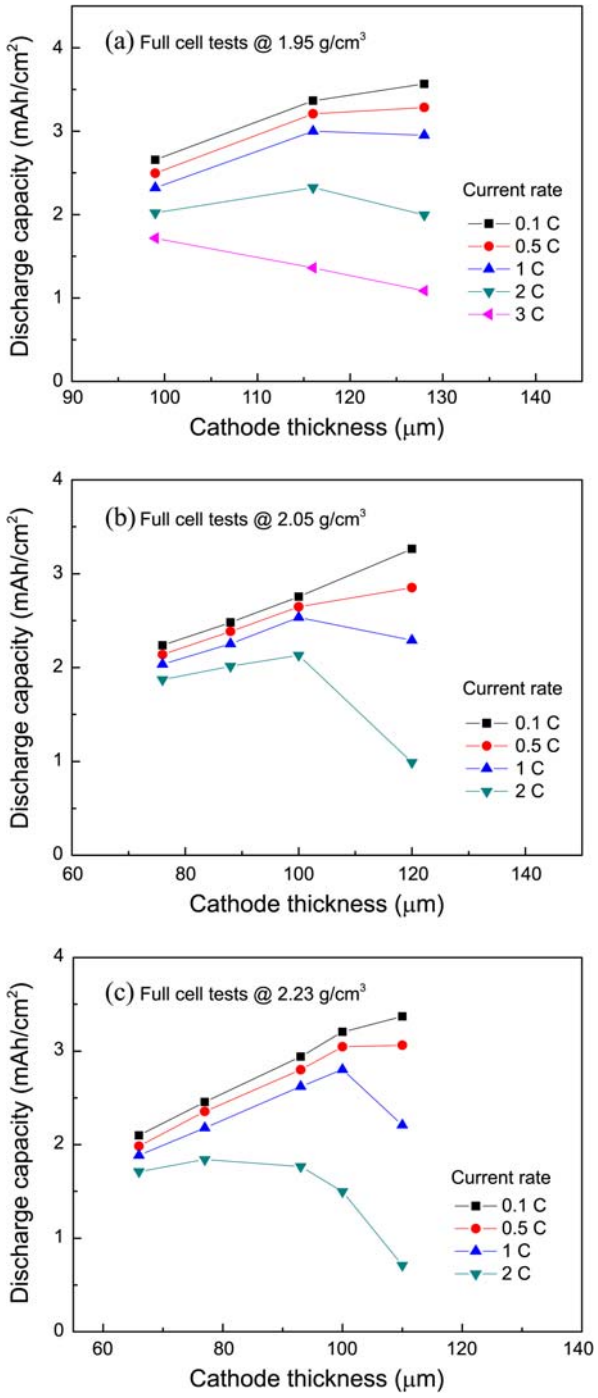

Figure 8. The measured discharge capacity per unit area (mAh/cm^2) for various cathode thicknesses and current rates: for the AM densities of (a) 1.95 g/cm^3, (b) 2.05 g/cm^3, and (c) 2.23 g/cm^3.

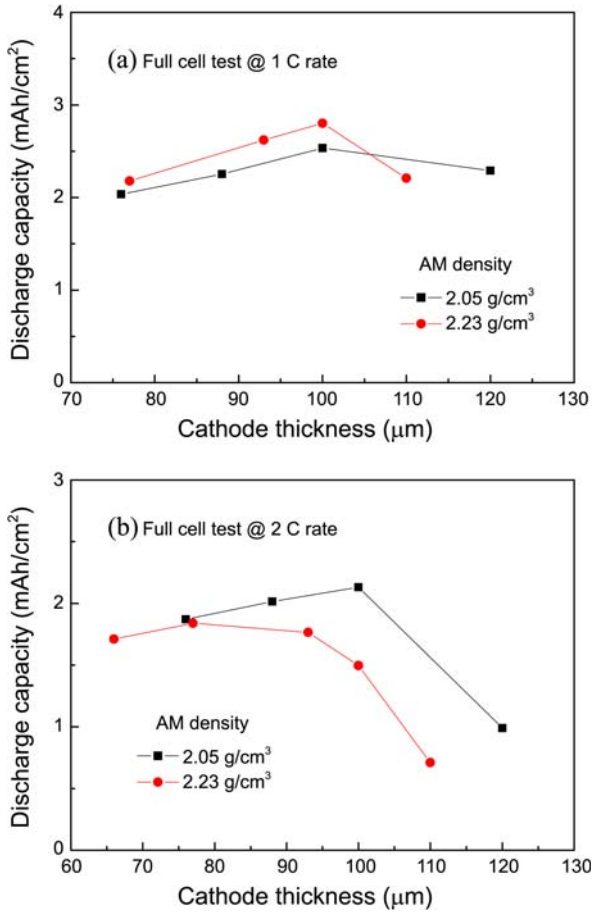

Figure 9. The measured discharge capacity as a function of the electrode thickness for the AM densities at of 2.05 and 2.23 g/cm^3 at the current rates of (a) 1 C and (b) 2 C.

these thicknesses, the discharge capacity can be maintained at high values of approximately 2.9 mAh/cm^2, 2.5 mAh/cm^2, and 2.5 mAh/cm^2 at a 1 C current rate and 2.2 mAh/cm^2, 2.0 mAh/cm^2, and 1.7 mAh/cm^2 at a 2 C current rate. Dense electrodes can greatly enhance the volumetric energy density needed to achieve the same area specific discharge capacity at the 1 C current rate. As the current rate increases, these dense electrodes also experience an increased capacity loss.

The AM density in the cathode is also an important design parameter that governs the discharge capacity. At a fixed cathode thickness of 100 μm, an analysis of Figure 8 indicated that the optimal AM density values were 2.23 g/cm^3, 2.05 g/cm^3 and 1.95 g/cm^3 for operating current rates of 0.5 C, 1 C, 2 C, and 3 C, respectively. This analysis suggests that a reduction in the AM density would increase the area specific discharge capacity for the high current rate applications. For low current rate applications, the dense and thick electrodes can be used to produce the highest discharge capacity. As shown in Figure 8(c), the discharge capacity with values as high as 3.4 mAh/cm^2 can be achieved with an electrode thickness of 110 μm and an AM density of 2.23 g/cm^3.

Figure 9 summarizes the trend of the discharge capacity as a function of the critical electrode thickness as measured from the cell tests. The discharge capacity trend shown in Figure 9 was similar to the values determined from the numerical simulations shown in Figure 4, although the estimated critical electrode thicknesses were different. In addition, the discharge capacity was also slightly different between the model prediction and the cell test results, by approximately 10%. The numerical model correctly predicted the important trend regarding the electrochemical phenomena, suggesting that this model may be useful as an efficient design tool for the development of electrochemical cells.

The discharge voltage curves measured from the cell tests at a 1 C rate, shown in Figure 10, were used to investigate the effects of the electrode thickness and the AM density. In Figure 10(a), the curves for a constant AM density of 2.05 g/cm^3 exhibit a slight voltage drop upon increasing the electrode thickness from 76 μm to 100 μm. The voltage drop increased rapidly as the electrode thickness exceeded the critical thickness of 110 μm, as determined from an analysis of Figure 8. The discharge voltage showed a decrease of approximately 0.2 V for an electrode thickness of 120 μm, with a reduction in the discharge capacity from 130 mAh/g

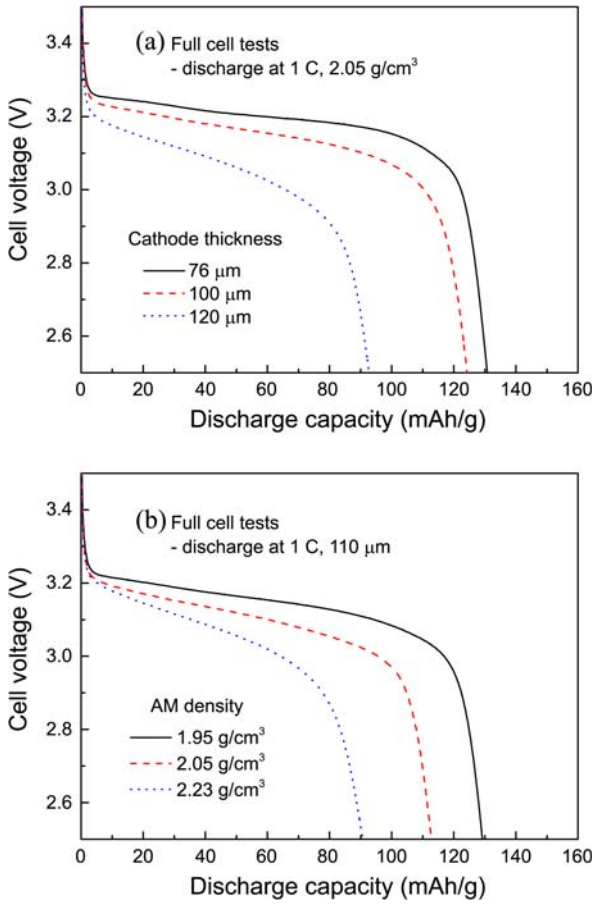

Figure 10. The measured discharge curves at the 1C current rate (a) for a constant AM density of 2.05 g/cm^3 and (b) for a constant electrode thickness of 110 μm.

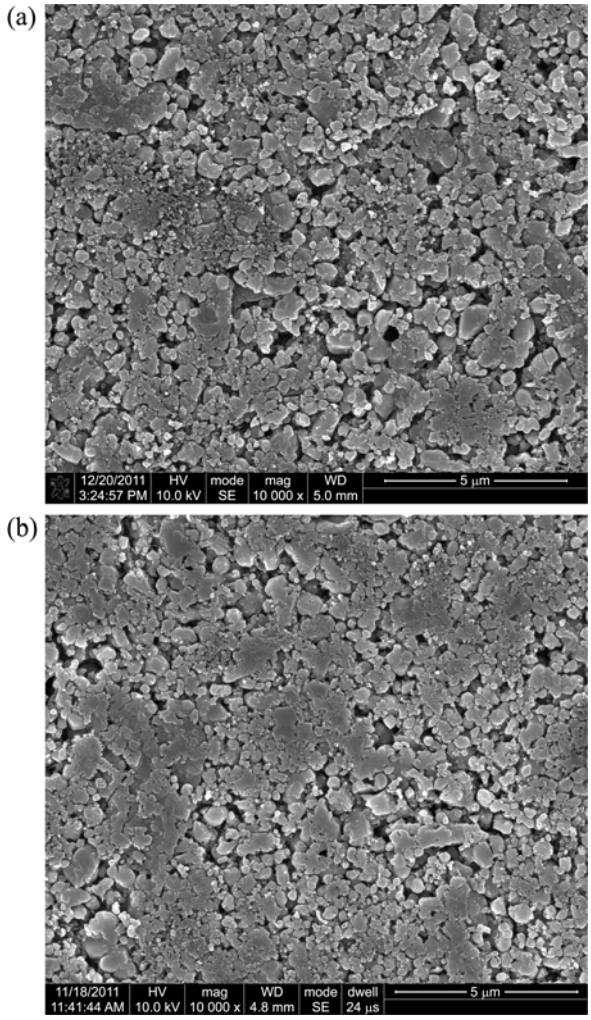

Figure 11. The SEM images of the $LiFePO_4$ electrodes at the AM densities of (a) 2.08 g/cm^3 and (b) 2.23 g/cm^3.

to 92 mAh/g due to the high ion transport limitations in the thick electrodes.

Figure 10(b) illustrates the discharge voltage curves for a constant electrode thickness of 110 μm for multiple AM densities. With increases in the AM density from 1.95 g/cm^3 and 2.23 g/cm^3, the voltage drop caused by the transport limitations in the electrolyte phase increased with a concomitant decrease in the discharge capacity from 130 mAh/g to 90 mAh/g. A value of the AM density higher than the optimal value can cause significant capacity loss, indicating that an optimization of the electrode thickness and AM density is necessary to achieve an increased capacity of the $LiFePO_4$/graphite lithium-ion batteries.

Figure 11 illustrates the SEM images (×10,000) of the $LiFePO_4$ electrodes for the AM densities of 2.08 g/cm^3 and 2.23 g/cm^3. As shown in Figure 11, the pore volume decreased and the transport paths increased in tortuosity with increasing AM density. The transport of the lithium ions in the electrode may not be problematic for low current rate operations. For high current rate operations, the lithium-ion transport through these tortuous paths can be significantly hindered, limiting the cell capacity. The AM density of 2.23 g/cm^3 is a high value that requires an approximately 45% compression of the initial electrode thickness during the fabrication process.

Conclusion

In this study, numerical simulations and experimental cell tests were performed to investigate the effects of the electrode thickness and the porosity (AM density) on the discharge performance of $LiFePO_4$/graphite electrodes, with the goal of producing high-capacity lithium-ion batteries. The numerical model parameters were determined by fitting the simulated discharge curves to the experimental curves recorded during the cell tests. The numerical simulation predicted that the area specific discharge capacity for a given AM density had a maximum capacity at a critical electrode thickness. A further increase of the electrode thickness above that critical thickness did not contribute to the capacity enhancement. From the simulation results, the critical thickness for the $LiFePO_4$ electrodes was estimated to be 110 μm for an AM density of 2.04 g/cm^3 and 95 μm for an AM density of 2.22 g/cm^3 at a 1 C current rate.

Cell tests were also conducted to examine the discharge capacity at thickness levels near the critical electrode thickness. The $LiFePO_4$/graphite lithium-ion batteries with cathode thickness values ranging from approximately 70 μm to 120 μm were fabricated using values of the AM density controlled at levels similar to those in the simulated conditions. The discharge capacity determined by the cell tests showed a similar trend to the values predicted from the numerical simulations, with slight differences in the estimated critical electrode thicknesses for the given AM density at a 1 C current rate as follows: 125 μm for 1.95 g/cm^3, 110 μm for 2.05 g/cm^3, and 100 μm for 2.23 g/cm^3. Based on the experimental results, the optimal cathode thickness was determined to be 115 μm, 100 μm, and 90 μm for the AM density values of 1.95 g/cm^3, 2.05 g/cm^3, and 2.23 g/cm^3, respectively. The $LiFePO_4$/graphite lithium-ion batteries with these electrode design parameters were observed to produce area specific discharge capacities greater than 2.5 mAh/cm^2 using a 1 C current rate.

The numerical simulation indicated that the lithium-ion transport limitations in the electrolyte phase were responsible for the capacity loss in the thick and the dense electrodes. For the thick and the dense cathodes, the voltage drop upon significant decreases in the lithium-ion concentration may cause the discharge voltage to reach the cut-off voltage values before the full utilization of the AM particles. The SEM images of the compressed electrodes were also inspected, demonstrating that the transport paths through the pores increased in tortuosity as a function of the compression. The highly compressed electrodes can result in significant transport limitations at high current rates by reducing the effective diffusivity and conductivity in the electrolyte phase.

Acknowledgments. This work was supported by the Energy Efficiency & Resources program of the Korea Institute of Energy Technology Evaluation and Planning (KETEP) grant funded by the Korea government Ministry of Knowledge Economy (20102010100090-11-2-200 and 20118510010030).

List of Symbols

a_i	Specific surface area of electrode i ($i = n, p$), m^{-1}
c	Electrolyte concentration, mol/m^3
c_s	Concentration of lithium in the AM particles of electrode i ($i = n, p$), mol/m^3
D	Diffusion coefficient of the lithium ions in the electrolyte, m^2/s
$D_{s,i}$	Diffusion coefficient of the lithium ions in the AM particles of electrode i ($i = n, p$), m^2/s
F	Faraday's constant, 96,487 C/mol
I	Applied current density, A/cm^2
j_i	Intercalation flux of lithium ions on the AM particles of the electrode i ($i = n, p$), mol/m^2-s
k_i	Reaction rate constant of electrode i ($i = n, p$), mol/(mol/m^3)$^{1.5}$
l_i	Thickness of the electrode i ($i = n, s, p$), m
n	Negative electrode
p	Positive electrode
r	Radial coordinate, m
R	Universal gas constant, 8.314 J/(mol-K)
R_i	Radius of the AM particles in electrode i ($i = n, p$), m
s	Separator
t_+	Transference number for the lithium ions in the electrolyte
T	Absolute temperature, K
U_i	Open-circuit potential of electrode i ($i = n, p$), V
x	Spatial coordinate, m, or degree of lithium-ion intercalation

Greek Letters

ε_i Porosity of the electrode i ($i = n, p$)
$\varepsilon_{f,i}$ Volume fraction of the fillers in electrode i ($i = n, p$)
$\varepsilon_{p,i}$ Volume fraction of the polymer in electrode i ($i = n, p$)
$\kappa_{eff,i}$ Effective ionic conductivity of the electrolyte phase in region i ($i = n, s, p$), S/m
σ_i Electronic conductivity of the solid phase in electrode i ($i = n, p$), S/m
$\sigma_{eff,i}$ Effective electronic conductivity of the solid phase in electrode i ($i = n, p$), S/m
Φ_1 Solid-phase potential, V
Φ_2 Electrolyte-phase potential, V

References

1. Huang, H.; Yin, S. C.; Nazar, L. F. *Electrochem. Solid State Lett*. **2001**, *4*, A170.
2. Chen, Z.; Dahn, J. R. *J. Electrochem. Soc.* **2002**, *149*, A1184.
3. Prosini, P. P.; Zane, D.; Pasquali, M. *Electrochim. Acta* **2001**, *46*, 3517.
4. Chung, S. Y.; Bloking, J. T.; Chiang, Y. M. *Nat. Mater*. **2002**, *1*, 123.
5. Wang, D.; Li, H.; Shi, S.; Huang, X.; Chen, L. *Electrochim. Acta* **2005**, *50*, 2955.
6. Shi, S.; Liu, L.; Ouyang, C.; Wang, D. S.; Wang, Z.; Chen, L.; Huang, X. *Phys. Rev. B* **2003**, *68*, 195108.
7. Sides, C. R.; Croce, F.; Young, V. Y.; Martion, C. R.; Scrosati, B. *Electrochem. Solid-State Lett.* **2005**, *8*, A484.
8. Kim, D. H.; Kim, J. *Electrochem. Solid-State Lett.* **2006**, *9*, A439.
9. Jiao, F.; Hill, A. H.; Harrison, A.; Berko, A.; Chadwick, A.; Bruce, P. G. *J. Am. Chem. Soc.* **2008**, *130*, 5262.
10. Dominko, R.; Bele, M.; Goupil, J. M.; Gaberscek, M.; Hanzel, D.; Arcon, I.; Jamnik, J. *Chem. Mater*. **2007**, *19*, 2960.
11. Yu, D. Y. W.; Donoue, K.; Inoue, T.; Fujimoto, M.; Fujitani, S. *J. Electrochem. Soc*. **2006**, *153*, 835.
12. Fongy, C.; Gaillot, A. C.; Jouanneau, S.; Guyomard, D.; Lestriez, B. *J. Electrochem. Soc*. **2010**, *157*, 885.
13. Gaberscek, M. *J. Power Sources* **2009**, *189*, 22.
14. Albertus, P.; Couts, J.; Srinivasan, V.; Newman, J. *J. Power Sources* **2008**, *183*, 771.
15. Nyman, A.; Zavalis, T. G.; Elger, R.; Behm, M.; Lindbergh, G. *J. Electrochem. Soc*. **2010**, *157*, A1236.
16. Chen, Y. H.; Wang, C. W.; Zhang, X.; Sastry, A. M. *J. Power Sources* **2010**, *195*, 2851.
17. Safaria, M.; Delacourt, C. *J. Electrochem. Soc*. **2011**, *158*, 63.
18. Doyle, M.; Fuller, T. F.; Newman, J. *J. Electrochem. Soc.* **1993**, *140*, 1526.
19. Fuller, T. F.; Doyle, M.; Newman, J. *J. Electrochem. Soc.* **1994**, *141*, 1.
20. Fuller, T. F.; Doyle, M.; Newman, J. *J. Electrochem. Soc.* **1994**, *141*, 982.
21. Doyle, M.; Newman, J. *J. Electrochem. Soc.* **1996**, *143*, 1890.
22. Srinivasan, V.; Newman, J. *J. Electrochem. Soc.* **2004**, *151*, 1517.
23. Srinivasan, V.; Newman, J. *J. Electrochem. Soc.* **2004**, *151*, 1530.
24. Singh, G. K.; Ceder, G.; Bazant, M. Z. *Electrochim. Acta* **2008**, *53*, 7599.
25. Tang, M.; Carter, W. C.; Chiang, Y. M. *Annu. Rev. Mater. Res.* **2010**, *40*, 501.
26. Tang, M.; Belak, J. F.; Dorr, M. R. *J. Phys. Chem. C* **2011**, *115*, 4922.